

How wind shear affects trade-wind cumulus convection

K. C. Helfer¹, L. Nuijens¹, S. R. de Roode¹, A. P. Siebesma^{1,2}

¹Department of Geoscience and Remote Sensing, Delft University of Technology, Delft, The Netherlands

²Royal Netherlands Meteorological Institute (KNMI), De Bilt, The Netherlands

Key Points:

- Shear in the zonal wind influences cloud-top heights via the effect of momentum transport on the surface wind and surface fluxes.
- Backward shear (surface easterlies turn westerlies) lowers cloud tops and shallows and moistens the trade-wind layer.
- Any absolute amount of wind shear limits in-cloud updraft speeds and enhances low-level cloud fraction.

Corresponding author: Kevin Helfer, k.c.helfer@tudelft.nl

Abstract

Motivated by an observed relationship between marine low cloud cover and surface wind speed, this study investigates how vertical wind shear affects trade-wind cumulus convection, including shallow cumulus and congestus with tops below the freezing level. We ran large-eddy simulations for an idealised case of trade-wind convection using different vertical shears in the zonal wind. Backward shear, whereby surface easterlies become upper westerlies, is effective at limiting vertical cloud development, which leads to a moister, shallower and cloudier trade-wind layer. Without shear or with forward shear, shallow convection tends to deepen more, but clouds tops are still limited under forward shear. A number of mechanisms explain the observed behaviour: First, shear leads to different surface wind speeds and, in turn, surface heat and moisture fluxes due to momentum transport, whereby the weakest surface wind speeds develop under backward shear. Second, a forward shear profile in the subcloud layer enhances moisture aggregation and leads to larger cloud clusters, but only on large domains that generally support cloud organization. Third, any absolute amount of shear across the cloud layer limits updraft speeds by enhancing the downward-oriented pressure perturbation force. Backward shear — the most typical shear found in the winter trades — can thus be argued a key ingredient at setting the typical structure of the trade-wind layer.

Plain Language Summary

We used a high-resolution weather model to investigate the influence of the shape of the wind profile (i.e. whether the wind blows faster, slower or with the same velocity at greater altitudes compared to the surface) on shallow cumulus clouds typical of the North Atlantic trade-wind region. In this region, easterly winds that decrease with height (and eventually turn westerly) are most common. Generally, the surface winds are also affected by how the wind blows further aloft, influencing what kind of clouds form. But even when we eliminate this effect in our study, we find that when the wind blows faster or slower at greater heights, clouds are not only tilted but also wider, and both effects increase the overall cloud cover. Furthermore, if the wind speed changes with height, the updraft speed within clouds is diminished, which potentially decreases the height of clouds. However, if the wind speed increases with height (which only rarely occurs in the trades), clouds tend to cluster more, which ‘offsets’ the weaker updrafts, and thus still allows for deeper clouds.

1 Introduction

In light of the uncertain role of trade-wind cumulus clouds in setting the cloud feedback in climate change, there is widespread interest in understanding the behaviour of these clouds, the different ways they interact with their environment and how this changes in response to global warming (e.g. Bony & Dufresne, 2005; Bony et al., 2013; Vial et al., 2017). Trade-wind cumuli are found in regions characterised by the trade winds, yet we understand relatively little about how they depend on the structure of the trade wind, compared to how they depend on temperature and moisture. Some studies have investigated the influence of the wind speed on low clouds in the trades and revealed that surface wind speed is one of the better predictors of low cloud amount (e.g. Nuijens & Stevens, 2012; Brueck et al., 2015; Klein et al., 2017). But it is unclear how much the wind shear plays a role in observed cloud amount–wind speed relationships, as one might expect both wind speed and wind shear to increase with larger meridional temperature gradients throughout the lower troposphere when assuming geostrophic and thermal wind balance. Furthermore, little work has concentrated on the influence of wind shear on convection, other than its role in increasing the amount of projected cloud cover.

From studies of deep convection we know that wind shear can have a number of effects. Shear is effective at organizing deep convective systems into rain bands and squall lines (e.g. Thorpe et al., 1982; Rotunno et al., 1988; D. J. Parker, 1996; Hildebrand, 1998; Robe & Emanuel, 2001; Weisman & Rotunno, 2004). At the same time, shear can limit convection during its developing stages (Pastushkov, 1975). A recent paper by Peters et al. (2019) clearly shows how shear reduces updraft speeds in slanted thermals by enhancing the (downward-oriented) pressure perturbations. Shear is also argued to inhibit deep convection by ‘blowing off’ cloud tops (e.g. Sathiyamoorthy et al., 2004; Koren et al., 2010), which we interpret as an increase in the cloud surface area that experiences entrainment, which also plays a role in setting updraft buoyancy and updraft speeds.

Malkus (1949) might have been one of the first to mention the effect of shear on shallow convection, noting that the tilting of clouds through shear causes an asymmetry in its turbulence structure with more turbulence on the windward than the leeward side. Through numerous studies we now know that shear helps organize shallow convective clouds in rolls or streets along with the development of coherent moisture and temperature structures in the subcloud layer (e.g. Malkus, 1963; Asai, 1964; Hill, 1968; LeMone

76 & Pennell, 1976; Park et al., 2018). Li et al. (2014) explain how shear over the subcloud
77 layer interacts with the low-level circulation induced by cold pools to enhance or limit
78 the regeneration of convective cells and longevity of shallow cloud systems. In a recent
79 LES study of shallow convection over the Sulu Sea in the Philippines, Yamaguchi et al.
80 (2019) find that wind shear leads to a stronger clustering of clouds and slightly increased
81 cloud-base cloud fractions as well as diminished cloud depths. Brown (1999) shows that
82 shear can strongly affect the surface wind via momentum transport, but that it has lit-
83 tle effect on the turbulence kinetic energy (TKE) budget, on scalar fluxes and on cloud
84 properties. This is in contrast to the dry convective boundary layer, where shear has a
85 strong impact on the TKE budget (Fedorovich & Conzemius, 2008, and references therein).

86 The present study investigates how vertical wind shear influences trade-wind cu-
87 mulus convection, including shallow cumulus and cumulus congestus below the freezing
88 level. For instance, we ask, how shear impacts cloud tops, cloud amount and the struc-
89 ture of the boundary layer. To this end, we used an idealised large-eddy-simulation (LES)
90 case — inspired by Bellon and Stevens (2012) and Vogel et al. (2016) and not unlike the
91 typical atmosphere in the trades — aiming at a fundamental understanding of the sen-
92 sitivity to forward and backward shear (by which we mean an increase and decrease, re-
93 spectively, of the zonal wind speed with height) of different strengths.

94 The remainder of this paper is structured as follows. We first explain our idealised
95 LES set-up and the wind shear variations we impose. The results are then presented in
96 a twofold manner. First, we discuss the effects of shear on the cloud and boundary-layer
97 evolution, showing results from large- and small-domain simulations with interactive and
98 prescribed surface fluxes. Second, focusing on the large-domain runs with constant sur-
99 face fluxes, we discuss how shear impacts the cloud structure and cloud depth without
100 surface flux responses. We end with a concluding discussion and an outlook on future
101 work. In an appendix, we discuss the influence of shear on the clouds' vertical-velocity
102 budget.

103 **2 Experimental design**

104 We carried out large-eddy simulations (LES) using version 4.2 of the Dutch Atmo-
105 spheric Large Eddy Simulation (DALES; Heus et al., 2010). In our experimental set-up,
106 we prescribed large-scale forcings and initial profiles typical of the North Atlantic trades

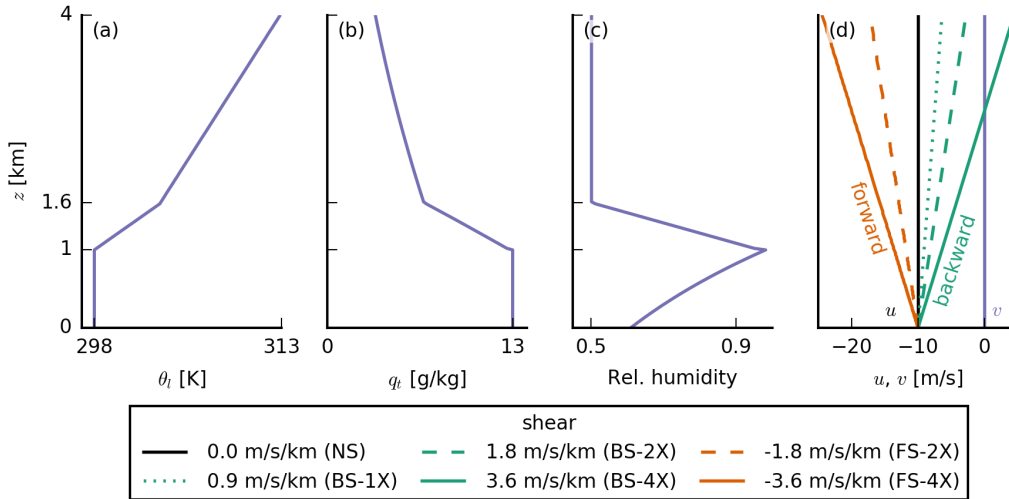


Figure 1. Initial profiles of (a) the liquid water potential temperature θ_l , (b) total water specific humidity q_t , (c) relative humidity and (d) the two wind components u and v . Purple profiles are the same in all simulations. Orange stands for forward shear (FS) and green for backward shear (BS). Same line types indicate the same amounts of absolute shear (1X, 2X, 4X). The colour coding of the different shears is the same for all other figures.

107 at a latitude of $\varphi = 15^\circ$ N (Sections 2.1–2.3). We used a domain of 50.4×50.4 km²,
 108 with a resolution of 100 m in the horizontal directions and doubly periodic boundary con-
 109 ditions. The domain top is at about 18 km and the vertical grid is non-uniform: start-
 110 ing with 10 m at the surface and increasing by a factor of 0.01 at each level to about 190 m
 111 at the domain top. In order to evaluate the effect of different surface winds and surface
 112 heat fluxes that develop under shear, we performed simulations with interactive and pre-
 113 scribed sensible and latent surface fluxes (Section 2.4). We also conducted simulations
 114 on a smaller domain (12.6×12.6 km²) where the development of cold pools and deeper
 115 clouds is less pronounced (Vogel et al., 2016).

116 2.1 Thermodynamics

117 The standard case set-up is inspired by that of Vogel et al. (2016) and Bellon and
 118 Stevens (2012), who introduced an idealised modeling framework with only a limited set
 119 of parameters that represent the large-scale flow. The initial temperature and humid-
 120 ity profiles of our simulations (Fig. 1) have a well-mixed layer of 1 km depth over a sur-
 121 face with a constant sea-surface temperature (SST) of 300 K. The mixed layer is topped

122 by a 600-m-deep inversion layer. In the free troposphere, the profile of liquid water po-
 123 tential temperature θ_l follows a constant lapse rate of 4 K/km, and the relative humid-
 124 ity is constant with height at 50 percent. We applied a constant radiative cooling rate
 125 of -2.5 K/d to θ_l (i.e. no diurnal cycle), which promotes relatively strong shallow con-
 126 vection, allowing for the development of the congestus clouds we are interested in. Com-
 127 pared to Vogel et al. (2016), we increased the domain top to 18 km to allow for deeper
 128 convection. Between 10 and 18 km, the radiative cooling is quadratically reduced to zero.
 129 The relative humidity reaches zero at about 14 km, which is also the lower boundary of
 130 the sponge layer in our LES. The θ_l lapse rate above 10 km is 8 K/km reflecting a sta-
 131 ble upper atmosphere. In all simulations, we used a single-moment ice microphysics scheme
 132 (Grabowski, 1998) and allowed for precipitation assuming a constant cloud droplet con-
 133 centration of 60 cm^{-3} .

134 2.2 Large-scale subsidence

135 Different than Vogel et al. (2016), we used a weak-temperature-gradient (WTG)
 136 assumption to calculate the subsidence profile, as the deeper congestus clouds that de-
 137 velop increasingly violate the assumption of a strongly subsiding atmosphere. Practically,
 138 the WTG method was implemented following Daleu et al. (2012): Above a reference height,
 139 we calculated the subsidence rate w_s such that it maintains the virtual potential tem-
 140 perature θ_v close to its initial (reference) profile $\theta_{v,0}$ according to

$$w_s = \frac{1}{\tau} \frac{\overline{\theta_v} - \theta_{v,0}}{\partial_z \theta_{v,0}}, \quad (1)$$

141 where the overbar indicates slab averaging, ∂_z symbolizes the vertical derivative and τ
 142 is the relaxation time scale, which can be thought of as the time scale over which den-
 143 sity anomalies are redistributed by gravity waves and thus how fast the circulation acts
 144 to counteract the heating induced by convection. We set $\tau = 1$ h, a rather short time
 145 scale that avoids the build-up of large density anomalies and unphysically high subsi-
 146 dence rates during episodes of deeper convection. WTG is not valid at levels where tur-
 147 bulence and convection effectively diffuse gravity waves. Therefore, we only apply WTG
 148 above 3 km, and below that (aligned with the bulk of the cloud layer above which cloud
 149 fraction becomes small), we linearly extrapolate w_s to zero. We also apply a nudging with
 150 a time scale of 6 h towards the initial q_t (total water specific humidity) profile in the free
 151 troposphere (above 4 km) to avoid spurious moisture tendencies.

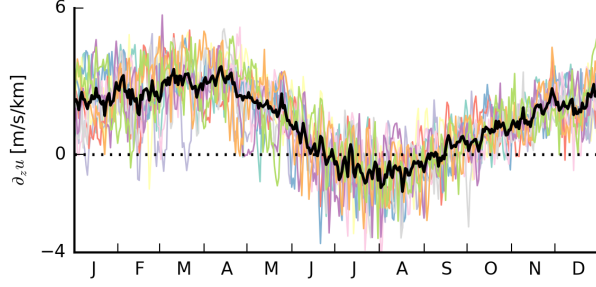


Figure 2. Time series of the amount of zonal shear between 1 and 3 km for the years 2008 to 2017 averaged over the area from 9° to 19° N and from 50° to 59° W (coloured lines). The black line is the average over all 10 years. The dotted horizontal line indicates 0 m/(s km). Data are from the ERA5 reanalysis.

152

2.3 Winds

153

154

The winds in our simulations are subjected to a large-scale forcing that involves only the pressure-gradient and Coriolis forces:

$$\left(\frac{du}{dt}\right)_{ls} = fv - \frac{1}{\rho} \frac{dp}{dx} = f(v - v_g), \quad (2)$$

$$\left(\frac{dv}{dt}\right)_{ls} = -fu - \frac{1}{\rho} \frac{dp}{dy} = -f(u - u_g), \quad (3)$$

155

156

157

158

159

160

161

162

where f is the Coriolis parameter, ρ the density, p the pressure, and u_g and v_g are the geostrophic winds. We use initial profiles of zonal and meridional winds that are equal to the imposed geostrophic wind ($u_0, v_0 = u_g, v_g$). We neglect large-scale horizontal wind advection, so that departures in the wind away from the geostrophic profiles are entirely due to the Coriolis force and the frictional force stemming from turbulence and convection. Because initially, the surface winds are in geostrophic balance, the simulation will undergo a transition towards ageostrophic surface winds (an Ekman balance). In this transition, the wind shear is effectively felt and adjusted through vertical mixing.

163

164

165

We based the wind profiles in our simulations on typical conditions in the trades, where vertical shear in the zonal wind component u is most common and to first order set by large-scale meridional temperature gradients through the thermal wind relation:

$$\frac{\partial u_g}{\partial z} \simeq -\frac{g}{fT} \frac{\partial T}{\partial y}, \quad (4)$$

166

167

where T the temperature and g the gravitational constant. In the northern hemisphere, temperature decreases poleward ($\partial_y T < 0$), so that $\partial_z u_g > 0$, which implies that winds

Table 1. Overview of the various LES experiments on a large ($50.4 \times 50.4 \text{ km}^2$) or small domain ($12.6 \times 12.6 \text{ km}^2$) and with interactive (constant SST) or fixed surface fluxes. For each set, we differentiate between runs without wind shear (NS), runs with weak (1X), medium (2X) or strong (4X) backward (BS) shear and runs with medium or strong forward (FS) shear (see also Fig. 1d).

Shear		NS	BS			FS	
			1X	2X	4X	2X	4X
acronym							
[10^{-3} s^{-1}]		0.0	+0.9	+1.8	+3.6	-1.8	-3.6
Large domain	interactive surface fluxes	✓	✓		✓		✓
	prescribed surface fluxes	✓	✓		✓		✓
Small domain	prescribed surface fluxes	✓	✓	✓	✓	✓	✓

168 become increasingly westerly (eastward) with height. $\partial_z u > 0$ is indeed typical for most
 169 of the year, as derived from daily ERA5 data (12:00 UTC) from 2008 to 2017 within 9° –
 170 19° N and 50° – 59° W (Fig. 2). In boreal summer, when the ITCZ is located in the north-
 171 ern hemisphere and meridional temperature differences within the subtropical belts are
 172 smaller, $\partial_z u$ is closer to zero or even negative. Vertical shear in the meridional wind com-
 173 ponent is close to zero year-round (not shown).

174 Further analysis of daily profiles (not shown) reveals substantial day-to-day vari-
 175 ability in the zonal wind profiles, regardless of the season, with reversals from negative
 176 to positive shear or zero shear from one day to the next, or vice versa. Forward shear
 177 (here $\partial_z u < 0$) is to some extent a frequent feature of the atmospheric flow in the trades
 178 — not only during summer. However, backward shear (here $\partial_z u > 0$) is still the most
 179 common.

180 The magnitude of shear we imposed in our simulations is not far from what we de-
 181 rived from ERA5. We ran simulations with different values of zonal shear, while setting
 182 $\partial_z v_g = 0$. The zonal wind profile has either no shear (NS, solid black line in Fig. 1d),
 183 forward shear (FS, $\partial_z u_g < 0$, orange lines) or backward shear (BS, $\partial_z u_g > 0$, green
 184 lines). The FS and BS simulations have different shear strengths ranging from $|\partial_z u_g| =$

185 $0.9 \times 10^{-3} \text{ s}^{-1}$ (1X, dotted line in Fig. 1d) over $|\partial_z u_g| = 1.8 \times 10^{-3} \text{ s}^{-1}$ (2X, dashed
 186 lines) to $|\partial_z u_g| = 3.6 \times 10^{-3} \text{ s}^{-1}$ (4X, solid coloured lines); see also Table 1.

187 The response to shear is not entirely insensitive to the choice of advection scheme.
 188 Here, scalar and momentum advection was performed using a 5th-order advection scheme
 189 in the horizontal direction and a 2nd-order advection scheme in the vertical direction.
 190 Using a 2nd-order scheme in the horizontal further increased the differences among the
 191 shear cases (in particular under free surface fluxes), which we attribute to the fact that
 192 the 2nd-order scheme accumulates a lot of energy on the smallest length scales close to
 193 the grid size. To reduce horizontal advective errors and allow for a larger time step, the
 194 grid was horizontally translated using a velocity that is equal to the imposed wind at
 195 3 km height (Galilean transform, see e.g. Wyant et al., 2018).

196 2.4 Surface fluxes

197 The control simulations were run for two days with interactive surface fluxes, which
 198 are parametrised using standard bulk flux formulae:

$$(\psi w)_s = -C_S U_1 (\psi_1 - \psi_s), \quad (5)$$

$$u_* = \sqrt{C_M} U_1, \quad (6)$$

199 where $\psi \in \{q_t, \theta_l\}$, U is the wind speed, u_* the surface friction velocity, and the sub-
 200 scripts s and 1 stand for the surface values and values on the first model level, respec-
 201 tively. The constants C_S and C_M are the drag coefficients, and they depend on the sta-
 202 bility and on the scalar and momentum roughness lengths, which we both set to $z_0 =$
 203 $1.6 \times 10^{-4} \text{ m}$. The drag coefficients are computed following Monin-Obukhov similar-
 204 ity theory (as described in Heus et al., 2010). Additionally, a set of experiments was con-
 205 ducted in which the surface fluxes were kept constant.

206 3 Impact of shear on cloud- and boundary-layer evolution

207 We first focus on the differences in cloud and boundary-layer structure that have
 208 developed by the end of a two-day simulation, using twelve-hourly averaged profiles (hour
 209 36–48), unless noted otherwise.

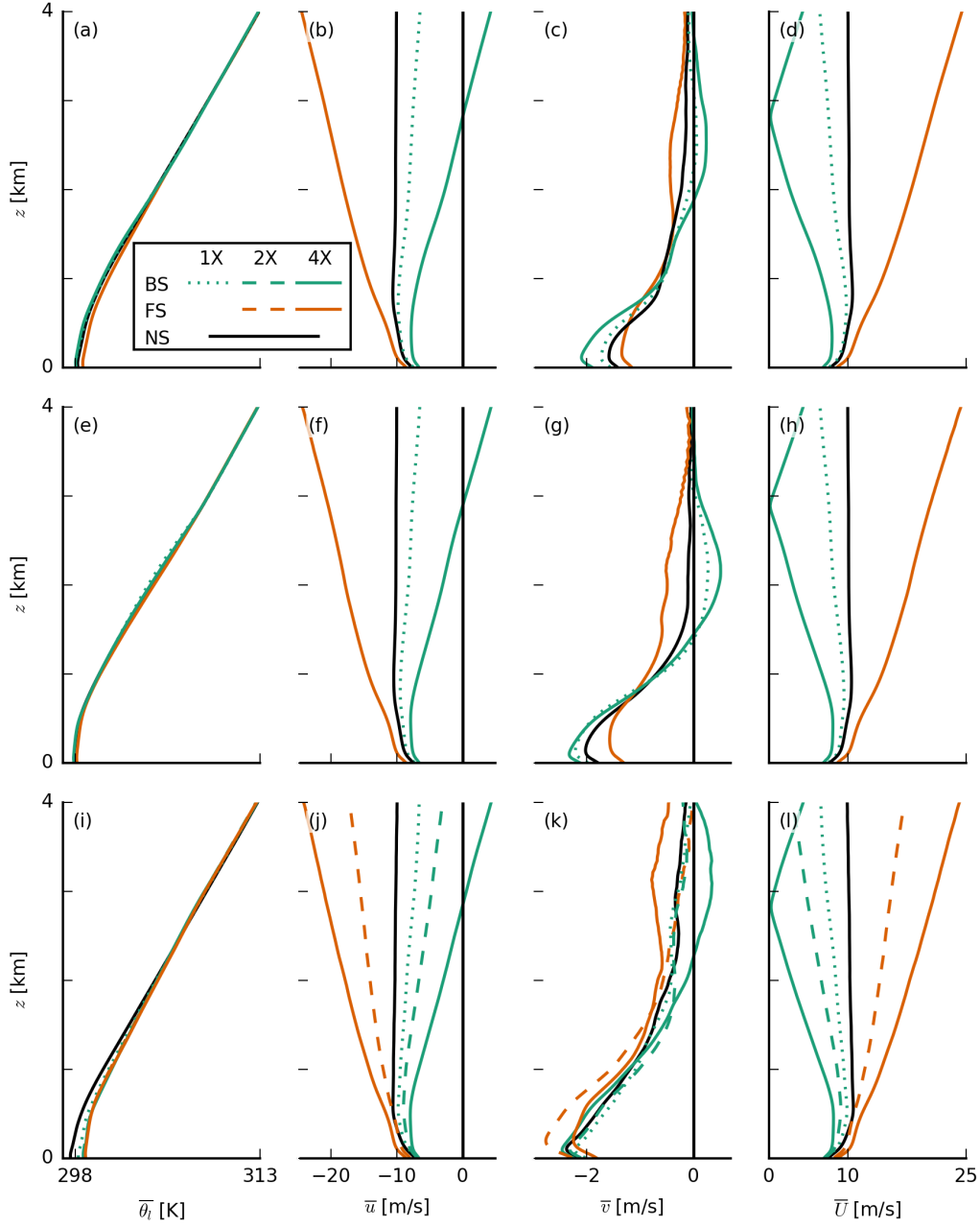


Figure 3. Slab-averaged profiles of thermodynamic quantities of the large-domain simulations with interactive surface fluxes (top row, a–d), with prescribed surface fluxes (middle row, e–h) and small-domain simulations (bottom row, i–l). Shown are averages over the last twelve hours of each simulation of (a, e, i) the liquid water potential temperature θ_l and (b, f, j) zonal, (c, g, k) meridional and (d, h, l) total wind speed, u , v and U , respectively. The line colours and types are explained in Fig. 1 and are the same in all following figures.

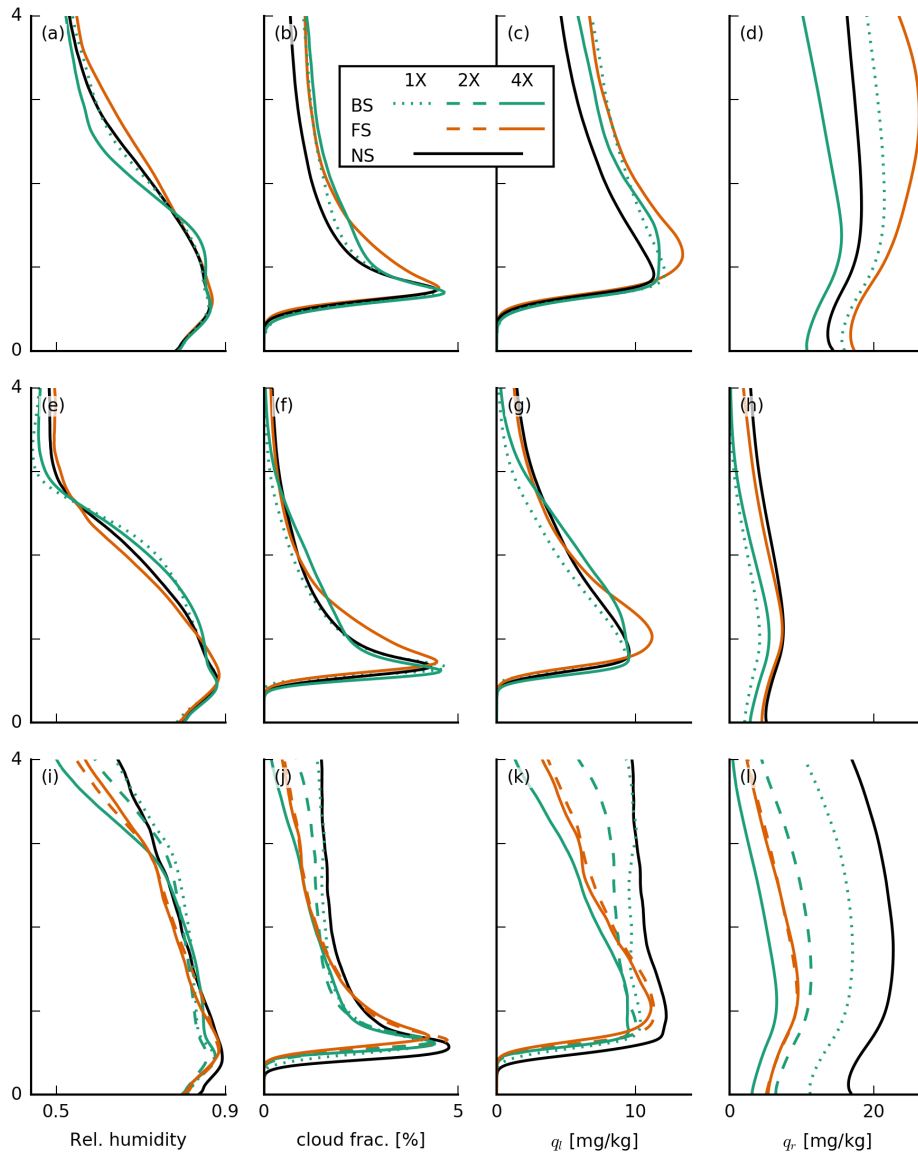


Figure 4. Slab-averaged profiles of thermodynamic quantities of the large-domain simulations with interactive surface fluxes (top row, a–d), with prescribed surface fluxes (middle row, e–h) and small-domain simulations (bottom row, i–l). Shown are averages over the last twelve hours of each simulation of (a, e, i) the relative humidity, (b, f, j) cloud fraction, (c, g, k) liquid water specific humidity q_l and (d, h, l) rain water specific humidity q_r .

210

3.1 Interactive surface fluxes

211

212

213

214

215

216

217

218

219

220

Similar to the findings of Brown (1999), who ran simulations for different wind shear on a very small domain ($6.4 \times 6.4 \text{ km}^2$), the influence of shear (Fig. 3b–d) on the thermodynamic structure of the boundary layer is overall marginal (Fig. 3a–b), but nonetheless evident in the relative humidity (RH), cloud fraction, liquid water and rain water profiles (Fig. 4a–d). In the presence of shear, regardless of its direction, cloud fractions above cloud base (approximately 700 m) are larger. In the FS-4X case the layer above 2 km is notably moister, whereas the BS-4X case has a more pronounced decrease of RH (which we interpret as the boundary-layer top) around 2 km. From strong backward to strong forward shear we thus observe a deepening of the moist layer and the disappearance of a pronounced hydrolapse.

221

222

223

224

225

226

227

228

229

230

231

232

233

234

235

Differences in the depth of convection are best seen from the rain water profiles (Fig. 4d) as well as the time series of average and maximum cloud-top heights (CTH), surface precipitation and low cloud cover, defined as the projected cloud amount from heights up to 4 km (Fig. 5a, c, e, g). Differences in cloud tops start to be pronounced only on the second day of the simulations, but looking closer, one can see that the highest cloud tops on day one are those of the FS-4X simulations (in orange). On day two, the NS simulation develops the deepest clouds with even an average cloud top near 7 km, whereas clouds in the simulations with shear, regardless of its sign, remain shallower and rain less. During the final twelve hours, clouds in all simulations show a pronounced deepening, and the FS-4X case even develops deeper clouds than the NS case, as well as more rain. Because we only use a simple single-moment ice microphysics scheme here, we are cautious with the interpretation of the cloud field when it deepens beyond the freezing level. Instead, we wish to focus on the deepening from shallow cumuli to congestus with tops near 4 km. Apparently, shear plays a role at hindering that development, in particular under BS.

236

237

238

239

240

241

Figure 5 shows that the surface heat fluxes play a key role in the deepening responses. Heat fluxes diverge very early on in the simulations, whereby the largest and smallest fluxes develop for the FS-4X and BS-4X cases, respectively (Fig. 5m, o). This exemplifies an important and perhaps often overlooked influence of wind shear. Given the same constant (geostrophic) forcing at the surface, a difference in zonal wind speeds can develop at the surface, due to the different zonal wind shear, which is felt near the surface

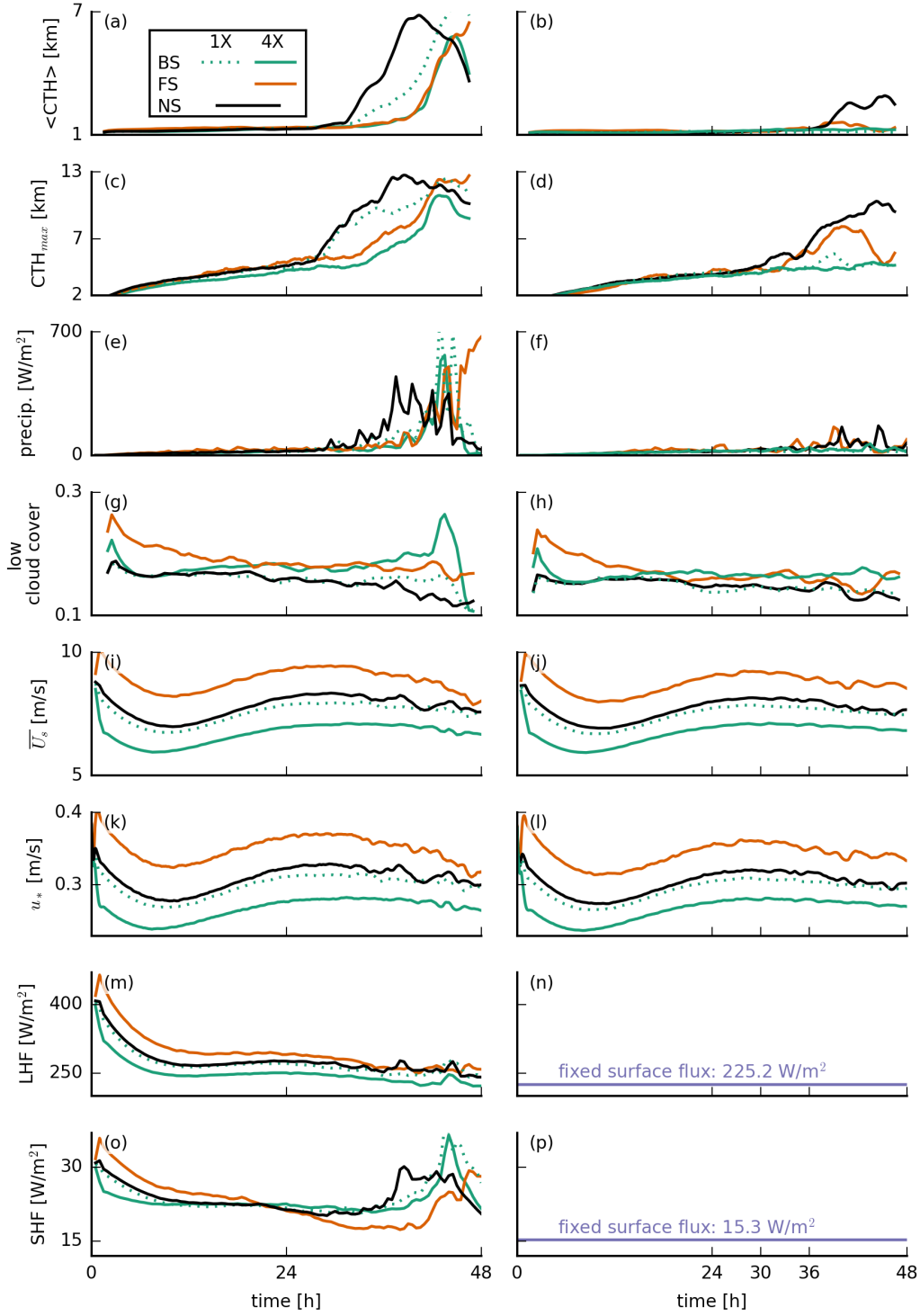


Figure 5. Time series of (a, b) the average and (c, d) the maximum cloud-top height (CTH), (e, f) the surface precipitation flux, (g, h) the low cloud cover ($z < 4$ km), (i, j) the domain-averaged total wind speed at 5 m height U_s , (k, l) the surface friction velocity u_* , (m, n) the surface latent heat flux LHF and (o, p) the surface sensible heat flux SHF for the interactive- (left column) and prescribed-surface-flux simulations (right column).

242 through turbulent mixing, at first, and then also through the Coriolis force as the wind
 243 starts to turn (see Eq. 2 and Fig. 3b–c). These differences in surface winds (Fig. 5i) give
 244 rise to the differences in surface fluxes (see Eq. 5).

245 As clouds deepen in all simulations during day two, the difference in surface heat
 246 fluxes becomes smaller, as downward mixing of warm and dry free tropospheric air re-
 247 duces the surface sensible heat flux while promoting the latent heat flux (Nuijens & Stevens,
 248 2012). The increase in the sensible heat fluxes in the final six hours may be attributed
 249 to precipitation and evaporative cooling of rain water in the subcloud layer (e.g. cold
 250 pools, Fig. 5e).

251 **3.2 Prescribed surface fluxes**

252 In light of these results, an important question is whether the surface fluxes are the
 253 only factor that plays a role in the development of convection, or whether shear has other
 254 more direct effects, including on the organization of clouds. Therefore, we carried out
 255 simulations with prescribed surface heat fluxes with relatively low magnitudes (namely
 256 $SHF = 15.3 \text{ W m}^{-2}$ and $LHF = 225.2 \text{ W m}^{-2}$, see the right column in Fig. 5 and
 257 second row in Figs. 3 and 4) as to minimize the development of very deep convection.
 258 Note that the surface friction (or surface momentum flux) is unchanged (Fig. 5k, l).

259 Apparently, the sensitivity of cloud deepening to shear does not change its over-
 260 all character when we prescribe the surface heat fluxes. Clouds are overall shallower with
 261 lower cloud fractions above 1 km (Fig. 4f, Fig. 5b, d), because the prescribed surface fluxes
 262 are smaller than in the interactive flux runs. But the FS-4X case still develops the largest
 263 relative humidities above the boundary layer ($>2.5 \text{ km}$), whereas the BS-4X case has the
 264 most pronounced hydrolapse near the boundary-layer top (Fig. 4e). Again the FS-4X
 265 case tends to produce somewhat deeper clouds during day one, but falls behind the NS
 266 case on day two. The BS-4X and BS-1X cases remain even shallower.

267 From previous studies (e.g. Malkus, 1949; Neggers et al., 2003; Yamaguchi et al.,
 268 2019) it is known that shear tilts clouds and thus increases cloud cover. In our FS and
 269 BS simulations, the tilt occurs in the negative and positive x direction, respectively, which
 270 enhances the low cloud cover by 10–20 % (Fig. 5g, h). A similar increase develops within
 271 a short time also after instantaneously introducing shear into a previously non-sheared
 272 system (Fig. 6c, discussed below). Besides this expected impact on cloud cover, there

273 are also some small differences in the cloud fraction profiles — including near cloud base,
 274 whose sensitivity has received much attention in recent climate studies (e.g. Vial et al.,
 275 2017; Bony et al., 2017). In the presence of shear, we observe a slightly larger maximum
 276 cloud fraction near cloud base (500–700 m) in the simulations with prescribed surface
 277 heat fluxes (Fig. 4b, f), in line with previous studies (e.g. Brown, 1999; Yamaguchi et
 278 al., 2019). BS-4X has a higher q_t variance at these heights, which are due to a few per-
 279 cent more active cloud (not shown) and which could explain the higher cloud fraction.
 280 In the FS-4X case, the larger cloud-base cloud fraction is explained by more passive cloud
 281 (not shown).

282 **3.3 Sensitivity tests on a smaller domain**

283 The same difference in deepening between the shear cases can be observed when
 284 applying instantaneous perturbations to the (geostrophic) wind shear, while keeping the
 285 surface fluxes constant (Fig. 6). In these sensitivity tests, carried out on a 16-fold smaller
 286 domain (see Table 1, which is still 4 times as large as the one used by Brown (1999)) we
 287 start from the equilibrium state of the NS case after two days, and then apply a pertur-
 288 bation. We then let the system evolve for another 36 hours. Also here it is evident that
 289 when wind shear is introduced, convective deepening is prevented (Fig. 6a–b) in com-
 290 parison with how the simulation develops without a perturbation (dashed black line in
 291 Fig. 6). Even very weak shear (BS-1X, dashed green line) can effectively reduce the clouds'
 292 depth and delay cloud deepening.

293 It is worthwhile to compare the profiles of RH and cloud fraction on the small do-
 294 main (Figs. 3i–l and 4i–l) with those on the large domain. The 16-fold smaller domain
 295 leads to much higher relative humidities and cloud fractions above 2 km. This can be
 296 explained by the lack of spatial organization of shallow convection on the small domain.
 297 Increasing the domain size generally tends to organize the shallow convection into deeper
 298 and larger clusters, which leads to a shallower, warmer and drier domain. Vogel et al.
 299 (2016) found that on a larger domain the likelihood of developing a strong updraft and
 300 deep cloud increases and that larger domains support stronger and deeper updrafts by
 301 allowing them to spread their compensating subsidence over a larger area. In the absence
 302 of spatial organization on the small domain, we can observe that only the FS-4X case
 303 behaves differently compared to the large domain. This case is no longer comparably moist
 304 or even moister than the NS case and its cloud fraction and RH profile is now more in

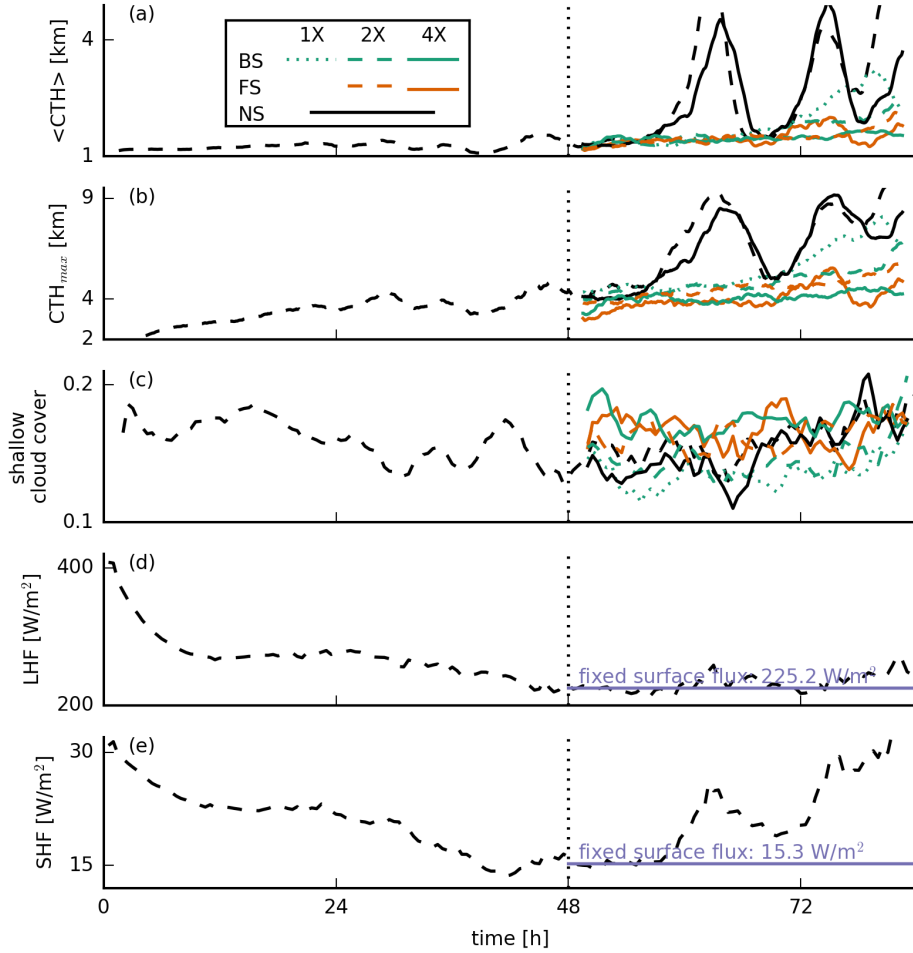


Figure 6. Time series of (a) the average and (b) the maximum cloud-top heights (CTH), (c) the low cloud cover ($z < 4$ km) and the (d) surface latent and (e) surface sensible heat fluxes for the small-domain simulations (48–84 h). In addition to the standard line types (see Fig. 1), the dashed black lines indicate a non-sheared simulation with interactive surface fluxes that is used to initialise the simulations at $t = 48$ h by perturbing the wind profiles and fixing the surface fluxes.

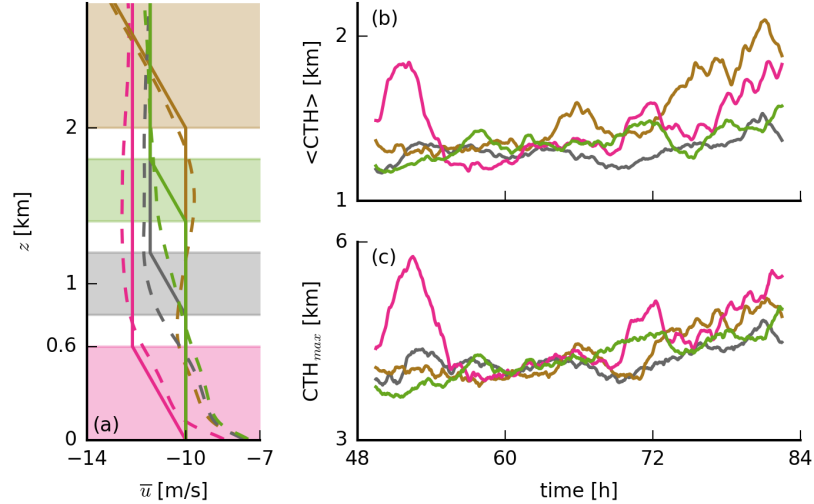


Figure 7. (a) Initial (solid lines) and slab-averaged profiles (from the last twelve hours; dashed lines) of the zonal wind u of simulations in which shear is only applied at limited height levels, as well as (b-c) the corresponding time series of the (b) average and (c) maximum cloud-top heights. Pink lines depict FS-4X shear at 0–0.6 km, grey at 0.8–1.2 km, green at 1.4–1.8 km and brown at 2–10 km.

305 line with that of the BS-4X case. This hints at a role of spatial organization in explain-
 306 ing the response to forward shear, which we address later.

307 Using the same experimental set-up (i.e. small domain, fixed surface fluxes and sud-
 308 den perturbation of the wind profile), we carried out some further sensitivity tests in which
 309 we applied forward shear to specific layers (Fig. 7). These simulations show that shear
 310 is particularly effective at keeping convection shallow when applied in the lower cloud
 311 layer (grey and green lines in Fig. 7), whereas shear in the subcloud layer (pink) or near
 312 cloud tops (brown) still leads to cloud deepening.

313 4 Sensitivity of convective deepening to shear

314 Overall, the previous section has shown that the presence of even weak backward
 315 shear effectively inhibits convective deepening, while forward shear only slightly weak-
 316 ens the potential to develop deeper clouds: This inhibition reveals itself as a delay (if sur-
 317 face feedbacks are present) or as a complete suppression of deepening (if surface heat fluxes
 318 are fixed). On a smaller domain, forward shear has the same strong inhibitive effect as

319 backward shear. If not through a surface flux response, what is the mechanism through
 320 which backward shear oppresses convection, while forward shear seems to allow for cloud
 321 deepening (on a sufficiently large domain)? Two hypotheses, borrowed from studies of
 322 deep convection, are as follows:

- 323 1. Wind shear changes the rate of entrainment, the updraft buoyancy and updraft
 324 speed: As clouds get tilted through any absolute amount of shear, they may suf-
 325 fer from more lateral entrainment and opposing pressure perturbations that limit
 326 updraft speeds and cloud vertical extent.
- 327 2. Wind shear changes the structure and organization of shallow cloud systems. For
 328 instance, forward shear helps to separate regions of updrafts and downdrafts and
 329 may therefore sustain larger subcloud circulations that continue to feed moisture
 330 into already cloudy areas. Forward shear may also interact with cold-pool fronts
 331 to force stronger updrafts.

332 To investigate these ideas, we consider only the simulations with prescribed surface fluxes
 333 and focus on the period between 30 and 36 h (unless noted otherwise). In this period,
 334 clouds first start to deepen from shallow cumulus to congestus at different rates depend-
 335 ing on shear, and the cloud field has not developed deep convection yet (cf. Fig. 5b, d).

336 **4.1 Entrainment and updraft speeds**

337 The FS-4X and BS-4X cases have significantly lower updraft speeds in the cloud
 338 cores ($q_l > 0$ and $\theta'_v > 0$) compared to the NS and BS-1X cases (Fig. 8a), which ap-
 339 pears key to explaining the lower cloud-top heights that develop under shear. However,
 340 the strongly sheared simulations contain nearly the same amount of cloud-core liquid wa-
 341 ter and are notably more buoyant, especially above 2 km (Fig. 8b, c). A similar picture
 342 is established if we sample on cloudy points ($q_l > 0$). Furthermore, the vertical mass
 343 flux is hardly affected by shear (not shown), as also found by Neggers et al. (2003). Buoy-
 344 ancy itself is evidently not key to explaining the weaker updrafts under shear (although
 345 it likely explains the stronger updrafts below 1 km in the BS-4X case). The relatively
 346 low buoyancy in cloud cores of the NS case (at least above 2 km) is because the envi-
 347 ronment surrounding the non-sheared clouds is warmer in terms of θ_v (not shown), be-
 348 cause clouds in that simulation are already mixing across a deeper layer (Fig. 5d), while
 349 the clouds themselves have a similar θ_v in each case. Vogel et al. (2016) also showed how

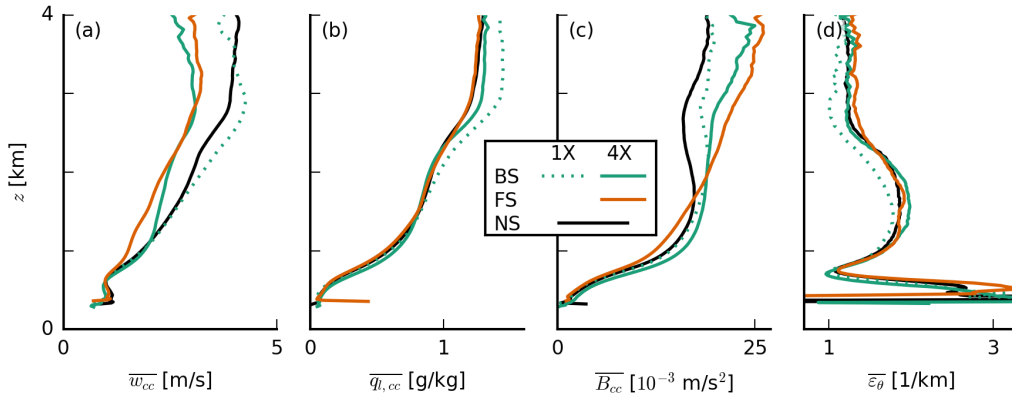


Figure 8. Slab-averaged profiles of (a) the cloud-core vertical velocity w_{cc} , (b) the cloud-core liquid water specific humidity $q_{l,cc}$, (c) the cloud-core buoyancy B_{cc} and (d) the fractional entrainment rate ε_{θ} of θ_l (averaged from 30 to 36 h of the simulations with prescribed surface fluxes).

350 quickly the thermodynamic structure of the boundary layer changes as shallow cumuli
 351 develop into cumulus congestus.

352 Using the simple entraining plume model by Betts (1975) to calculate the fractional
 353 entrainment rate ε_{θ} of θ_l (Fig. 8d), we find that clouds in the BS and FS cases entrain
 354 only marginally more environmental air than in the NS case if anything (also if we con-
 355 sider entrainment of q_t , not shown). This suggests that there is no larger lateral entrain-
 356 ment due to shear that could explain weaker vertical development. We also find that lat-
 357 eral entrainment plays a relatively small role in the conditionally sampled vertical-velocity
 358 budget (Appendix A).

359 The weaker cloud-core vertical velocities under shear are in line with studies of deep
 360 convection in squall lines, in particular the recent study by Peters et al. (2019) and ear-
 361 lier work by similar authors (M. D. Parker, 2010; Peters, 2016), who show that slanted
 362 updrafts are weaker than upright ones. Peters et al. (2019) decompose the vertical mo-
 363 mentum equation into four terms that describe the processes that regulate the vertical
 364 acceleration of updrafts: (1) a term associated with momentum entrainment and detrain-
 365 ment, (2) a (downward-oriented) dynamic pressure acceleration term, (3) a (downward-
 366 oriented) buoyancy pressure acceleration term and (4) a buoyancy acceleration term (which
 367 includes the entrainment of thermodynamic properties that can limit updraft buoyancy).

368 They show that shear mostly enhances the dynamic pressure perturbations, which can
 369 be interpreted as an aerodynamic lift force due to the shear-driven crossflow (perpen-
 370 dicular to the direction of ascent). Unlike the lift associated with aircraft wings, the lift
 371 in slanted thermals experiencing crossflow is directed downward. A handful of studies
 372 on the vertical-velocity budget of shallow convection have also noted a minor role of en-
 373 trainment in explaining updraft speeds (e.g. de Roode et al., 2012; Romps & Charn, 2015;
 374 Morrison & Peters, 2018; Tian et al., 2019).

375 An investigation of the vertical-velocity budget — a subject on its own as demon-
 376 strated by the aforementioned studies — goes beyond our goal, but we can get an im-
 377 pression of the importance of the pressure perturbations by sampling the vertical-velocity
 378 budget in cloudy updrafts, following de Roode et al. (2012), here included in Appendix
 379 A. We find that differences that contribute to the vertical velocity in the cloud layer are
 380 predominantly found in the pressure-gradient and buoyancy terms, whereas differences
 381 in the horizontal flux of resolved and subgrid vertical momentum across the cloud bound-
 382 aries (e.g. entrainment) are only important near cloud base (< 1 km) where other ten-
 383 dencies are small. Near cloud tops (> 2 km), updrafts in the sheared runs experience
 384 a larger negative pressure-gradient force. A quick look at the total pressure perturba-
 385 tions in x - z cross sections also confirms that pressure perturbations, especially near the
 386 slanted sides and tops of the clouds, are more pronounced under shear (not shown).

387 Overall, our results emphasise that shear keeps clouds shallower by weakening up-
 388 drafts. However, we also observe that clouds under forward shear have a tendency to get
 389 deeper than under backward shear. This is explored next.

390 **4.2 Structure and organization of turbulence and clouds**

391 In Fig. 9 we show a number of quantities that reveal changes to the character of
 392 the turbulence structure of the boundary layer: the domain-averaged variances of the
 393 velocity components, the turbulence kinetic energy (TKE), the skewness S and third cen-
 394 tral moment of the vertical velocity $\overline{w'^3}$ and finally the zonal and meridional momentum
 395 fluxes. Velocity variances are clearly enhanced in the FS-4X case, where the vertical gra-
 396 dient in wind speed between the surface and cloud tops — the shear — is largest (cf. Fig 3f-
 397 h). Consequently, TKE and the momentum fluxes are larger, in agreement with Brown

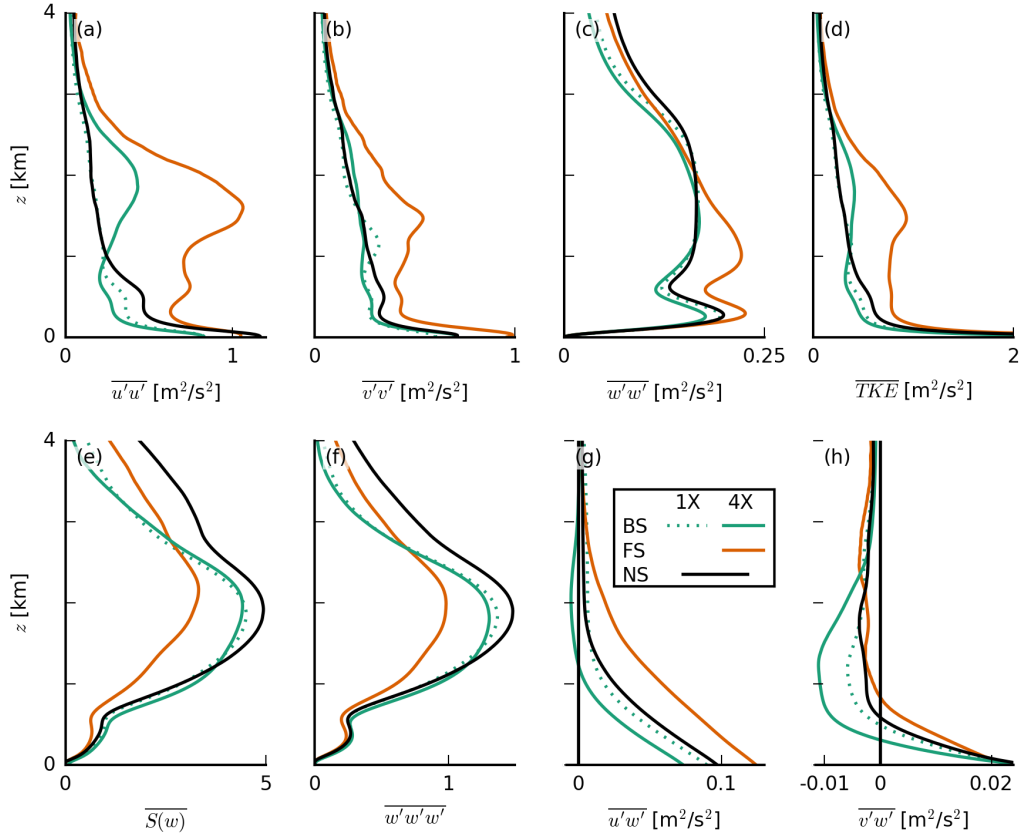


Figure 9. Slab-averaged profiles of the resolved variances of (a) the zonal wind speed $u'u'$, (b) the meridional wind speed $v'v'$ and (c) the vertical velocity $w'w'$, (d) the turbulence kinetic energy (TKE), (e) the skewness $S(w)$, (f) the third moment $w'w'w'$ of the vertical velocity and (g) the zonal and (h) the meridional momentum fluxes, $u'w'$ and $v'w'$, respectively (averaged from 30 to 36 h of the simulations with prescribed surface fluxes).

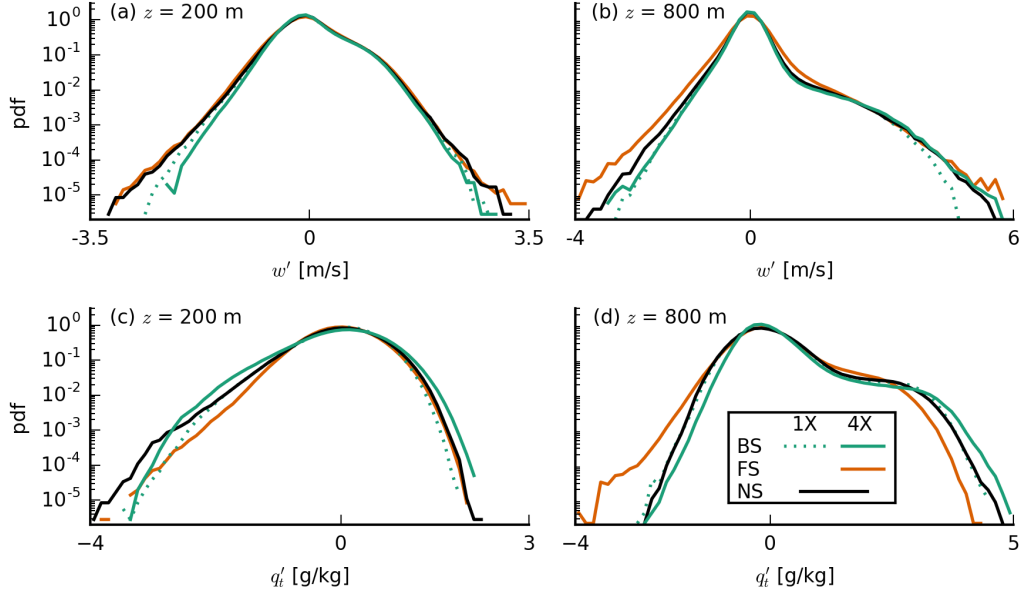


Figure 10. Probability density functions of the vertical velocity w (top) and the total water specific humidity deviations q'_t (bottom) at constant heights of (left) $z = 200$ m and (right) $z = 800$ m (averaged from 30 to 36 h of the simulations with prescribed surface fluxes).

398 (1999). Momentum fluxes at the surface are also largest for the FS-4X case, leading to
 399 a larger surface friction (see also Fig. 5i, j) and larger surface-layer shear.

400 Several authors have noted that convection can transition from a closed-cell struc-
 401 ture to roll structures due to shear (e.g. Sykes & Henn, 1989; Khanna & Brasseur, 1998;
 402 Salesky et al., 2017). A parameter that controls this transition is the ratio of the sur-
 403 face friction velocity u_* to the convective velocity scale w_* (Sykes & Henn, 1989) or equiv-
 404 alently the ratio of the Obukhov length and the boundary-layer height. While the ex-
 405 act value of u_*/w_* at which the transition takes place depends on other properties of the
 406 flow (different studies report values between 0.27 and 0.65), low values are clearly asso-
 407 ciated with cellular convection and high values with roll structures (Fedorovich & Conzemius,
 408 2008; Salesky et al., 2017). In our simulations, u_*/w_* has rather low values, which do
 409 not differ greatly among the various shear cases (ranging from about 0.30 for BS-4X to
 410 0.37 for FS-4X), indicating that convection is mainly buoyancy- and not shear-driven in
 411 all our simulations.

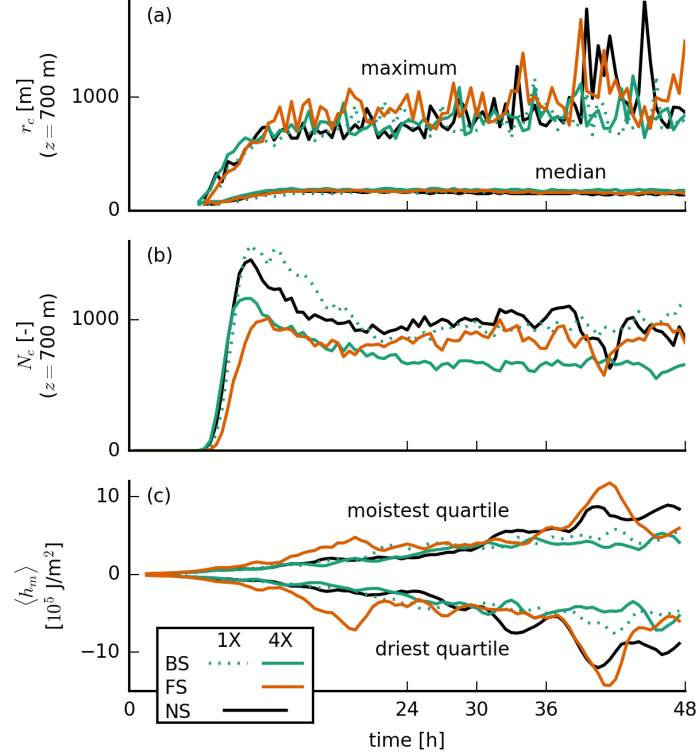


Figure 11. Time series of (a) the median and maximum cloud radius r_c at $z = 700$ m, (b) the number of clouds N_c at that height and (c) the vertically integrated moist static energy anomalies $\langle h_m \rangle$ in the moistest and the driest quartiles of 12.6×12.6 km² blocks for the simulations with prescribed surface fluxes.

412 The skewness of the vertical velocity $S(w) = \overline{w'^3}/\overline{w'^2}^{3/2}$, which is a measure for
 413 the asymmetry of the vertical velocity distribution, is reduced with FS. This is primar-
 414 ily caused by the reduction in the advection of vertical velocity variance, $\overline{w'^3}$, due to on
 415 average weaker updrafts into the cloud layer (Fig. 8a). The variance of w instead is larger
 416 under FS-4X (Fig. 9c). Although the PDFs of w at 200 m and at 800 m (near cloud base)
 417 in Fig. 10a–b are overall very similar, the FS-4X case has notably stronger updrafts as
 418 well as stronger downdrafts (tails of the PDF). This might be a signature of the down-
 419 drafts being separated from the updraft regions. Because the FS-4X case also has the
 420 largest absolute amount of wind shear across the subcloud layer, it has the largest posi-
 421 tive (anticlockwise) vorticity. These results suggest that instead of narrow updrafts closely
 422 surrounded by subsidence, the FS-4X case develops stronger ascent and descent in sep-
 423 arated branches of a circulation that enhances moisture transport into cloudy areas.

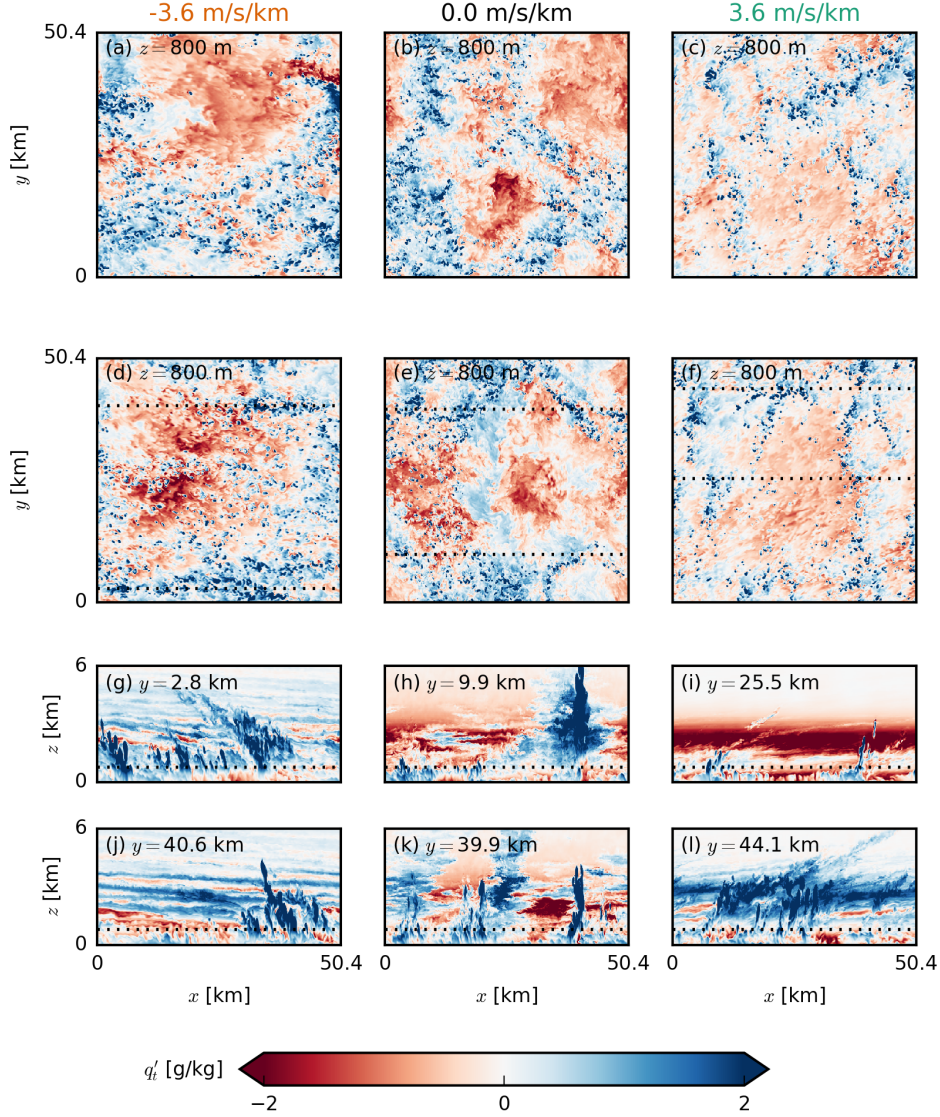


Figure 12. Snapshots of the LES domains of FS-4X (left), NS (centre) and BS-4X (right) exhibiting typical characteristics in the late stages of the simulations with prescribed surface fluxes. The top two rows (a–f) show horizontal x - y cross sections at two times ($t = 39.0$ h and $t = 46.5$ h) near cloud base ($z = 800$ m) of the deviations from the mean of the total water specific humidity q'_t . The bottom two rows (g–l) show corresponding vertical x - z cross sections from the lowest 6 km of the domain of the latter of the two times (d–f). The horizontal dotted lines indicate the position of the respective other cross sections.

424 Indeed, the FS-4X case has the largest amount of domain-averaged liquid water and
 425 cloud fraction between 800 m and 1.5 km on both small and large domains (Fig. 4f, g,
 426 j, k) and larger relative humidities just above cloud base (Fig. 4e, i), even though cloud
 427 base is on average higher than for the BS and NS cases. By analysing the mean and max-
 428 imum cloud radii and the number of clouds, we also find that the FS-4X case develops
 429 the fewest but the largest clouds (Fig. 11a, b), whereas the NS case has more numerous
 430 smaller clouds, similar to findings by Yamaguchi et al. (2019).

431 The formation or aggregation of larger clouds is also evident from the moisture field.
 432 Figure 11c shows deviations of the vertically integrated moist static energy within blocks
 433 of $12.6 \times 12.6 \text{ km}^2$ compared to the domain mean, and compares the moistest and the
 434 driest quartiles of the domain (in terms of total water path), which is a common mea-
 435 sure for self-aggregation (Bretherton & Blossey, 2017). This reveals that during the first
 436 24 h the strongest moistening of the moist regions and strongest drying of the dry re-
 437 gions takes place in the FS-4X cases. Furthermore, snapshots of the moisture field (Fig. 12)
 438 show that large patches of high or low moisture are less common in the simulations with
 439 backward shear compared to the other cases.

440 After the first day of simulation when precipitation increases, cold-pool effects might
 441 play an additional role in organizing the cloud and moisture field. The cold-pool bound-
 442 aries may interact with the environmental shear in the subcloud layer to trigger stronger
 443 force-lifted updrafts under FS (e.g. Li et al., 2014). The FS and BS cases also have a
 444 different wind speed distribution within the cold pools (Fig. 13). Whereas the BS case
 445 reveals the typical diverging flow with a strong easterly current left from the cold pool
 446 center and relatively stronger westerly winds towards the right, the FS case has much
 447 stronger easterly winds throughout. This may signify a role of downward momentum trans-
 448 port as well. The role of cold pool–shear interaction is the subject of a follow-up study.

449 5 Conclusions

450 In this paper, we have used idealised large-eddy simulations initialized and forced
 451 with a geostrophic wind that is equal at the surface, but has a different vertical profile
 452 (vertical wind shear). We showed that vertical wind shear influences the depth and char-
 453 acteristics of shallow cumulus convection, and thereby the depth and structure of the trade-
 454 wind layer. Even weak vertical shear in the zonal wind component can retard the growth

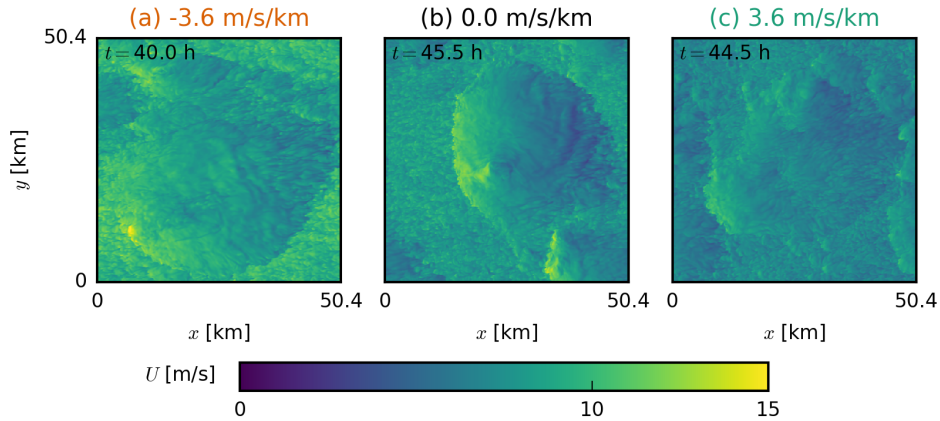


Figure 13. Snapshots of the LES domains of (a) FS-4X, (b) NS and (c) BS-4X exhibiting typical characteristics of the total wind speed U in the late stages of the simulations with prescribed surface fluxes. Shown are horizontal x - y cross sections at $z = 5$ m.

455 of cumulus clouds, in particular when the shear vector is directed against the mean wind
 456 direction (backward shear). Furthermore, we have shown that shear increases the cloud
 457 fraction — an effect that has been of major interest in recent climate studies (e.g. Vial
 458 et al., 2017; Bony et al., 2017).

459 Backward shear, whereby surface easterlies become upper westerlies, is typical for
 460 the winter trades, presumably because this season has a larger meridional temperature
 461 gradient between the equator and subtropics. Simulations with interactive surface fluxes
 462 reveal that backward shear can slow down vertical cloud development. Under backward
 463 shear, mean cloud tops remain near 2 km for at least 36 hours of simulation, at which
 464 point the simulations without (imposed) shear have developed clouds with mean tops
 465 near 7 km. Given the same geostrophic wind forcing at the surface, and in absence of
 466 horizontal wind advection, the weakest surface winds develop under backward shear. When
 467 initialising the simulations with surface winds in geostrophic balance, and no horizon-
 468 tal wind advection is applied, the weakest surface winds are reached under backward shear
 469 as the simulation approaches an Ekman balance: Relatively weaker wind speeds are then
 470 mixed towards the surface, compared to the simulations with forward shear or no shear.

471 Weak shear and forward shear (easterlies become stronger with height) are not un-
 472 common during boreal winter, even if they are more typical for boreal summer when the

473 ITCZ and deep convection shift northward. The vertical development of clouds under
474 forward shear is also delayed, but not as much as with backward shear, because simu-
475 lations with forward shear develop the strongest surface winds and (initially) the largest
476 surface heat fluxes.

477 To elucidate more direct effects of vertical shear, we repeated the simulations with
478 prescribed surface heat fluxes. These show that the presence of shear in the cloud layer,
479 regardless of its sign, limits updraft speeds, in line with studies of deep convection that
480 have shown shear to inhibit convective development (e.g. Peters et al., 2019). Entrain-
481 ment appears to play a minor role in setting the weaker updrafts (e.g. de Roode et al.,
482 2012; Romps & Charn, 2015; Morrison & Peters, 2018; Tian et al., 2019). Instead, larger
483 downward-oriented pressure perturbations under both forward and backward shear ap-
484 pear to weaken vertical accelerations.

485 In addition, shear changes the turbulence structure of the subcloud layer. Though
486 our simulations remain buoyancy-driven and do not develop roll structures or cloud streets,
487 forward shear develops stronger updrafts and downdrafts, a moister layer near cloud base
488 with larger cloud fraction, fewer but larger cloud clusters and more moisture aggrega-
489 tion. Forward shear maintains the largest absolute amount of shear in the sub-cloud layer,
490 which leads to a larger background vorticity and separates regions with updrafts from
491 regions with downdrafts. This may develop a stronger subcloud circulation with sustained
492 regions of ascending motion that feed moisture into areas of clouds. The larger cloud clus-
493 ters can become deeper, as they do in the first day of simulation under forward shear,
494 but are ultimately limited by weaker updraft speeds.

495 As clouds remain shallower under backward shear, the moistening of the cloud layer
496 is more pronounced and the top of the cloud layer is marked by a steeper decrease in hu-
497 midity, as is typical near the trade-wind inversion (e.g. Riehl et al., 1951). The moister
498 subcloud and cloud layer, as well as a stronger inversion, will lead to more cloudiness.
499 Therefore, we may argue that the trade winds themselves help to set the trade-wind in-
500 version and thus that backward shear is a crucial ingredient in defining the typical trade-
501 wind-layer structure.

Appendix A Impact of shear on the vertical-velocity budget

To study a difference in the forcing acting on the vertical velocity of cloudy updrafts in simulations with and without shear we follow the method by de Roode et al. (2012) who applied the top-hat approach by Siebesma and Cuijpers (1995) to compute the conditionally sampled vertical-velocity budget in DALES:

$$\frac{\partial w_c}{\partial t} = \underbrace{\frac{g(\theta_{v,c} - \overline{\theta_v})}{\theta_0}}_B - \underbrace{\left[\frac{\partial \pi}{\partial z} \right]_c}_P + \underbrace{2\Omega \cos \varphi u_c}_C - \underbrace{\frac{1}{2\rho} \frac{\partial w_c^2}{\partial z}}_A - \underbrace{\frac{1}{\rho \sigma_c} \frac{\partial \sigma_c \overline{w'' w''^c}}{\partial z}}_{S_p} - \underbrace{\frac{\epsilon_w w_c^2}{1 - \sigma}}_E, \quad (\text{A1})$$

where the subscript c stands for conditional sampling (here: on cloudy updrafts, i.e. $q_l > 0$ and $w > 0$), g the gravitational acceleration, θ_v the virtual potential temperature, θ_0 a reference temperature, π the modified pressure, Ω Earth's angular velocity, φ the latitude, σ the area fraction, ϵ_w the fractional entrainment rate of w and ρ the slab-mean density. The modified pressure π is defined as

$$\pi = \frac{1}{\rho} (p - \overline{p_h}) + \frac{2}{3}e, \quad (\text{A2})$$

where p is the pressure, p_h the hydrostatic pressure and e the subgrid-scale TKE. The latter is included because in DALES, $\frac{2}{3}e$ is subtracted from the subgrid momentum flux to simplify its computation; to compensate for this, the term is added back to the pressure (Heus et al., 2010). Preliminary tests show, however, that the subgrid TKE contribution to the conditionally sampled pressure term is small and insensitive to shear (not shown). The tendency on the l.h.s. of Eq. A1 is calculated directly from the LES. Averaged over six hours (30 to 36 h) it is close to zero. This tendency closely matches the sum of the terms on the r.h.s., which represent the buoyancy acceleration (B), the vertical pressure gradient (P), the Coriolis force (C), the vertical advection (A), the subplume vertical advection (S_p), and the lateral entrainment E .

Above 1 km, in the cloud layer, the production of vertical velocity from positive buoyancy B is largely balanced by a sink of vertical velocity due to the pressure gradient P , followed by a smaller sink from advection A . The subplume term S_p is close to zero in the cloud layer, and C is also small (negative). The lateral entrainment term E is small yet positive, counter to the conventional idea that entrainment is contributing negatively to cloud updraft quantities. This unexpected sign of the diagnosed lateral entrainment rate was also observed by de Roode et al. (2012) who argued that changes in the number of sampled points as parcels enter or leave cloudy updrafts (so-called Leibniz terms) may violate the implicit assumption that lateral entrainment is dominated

531 by horizontal advection. As Young (1988) explained, any sampled derivative, such as of
 532 vertical velocity,

$$\left[\frac{\partial w}{\partial t} \right]_c = \frac{\partial w_c}{\partial t} + \frac{w_c}{\sigma} \frac{\partial \sigma}{\partial t} + \left\{ \frac{\partial w}{\partial t} \right\}_L, \quad (\text{A3})$$

533 introduce an additional term that stems from Leibniz's rule of differentiation. It repre-
 534 sents temporal changes in the sampled vertical velocity due to changes in the sampling
 535 set. To let the lateral entrainment term in Eq. A1 be consistent with parametrised vertical-
 536 velocity equations (see Eq. 3 in de Roode et al., 2012), we diagnosed it as

$$-\frac{\epsilon_w w_c^2}{1 - \sigma} = -\frac{w_c}{\sigma} \frac{\partial \sigma}{\partial t} - \frac{w_c}{\sigma} \frac{\partial M_c}{\partial z} - \left[\frac{\partial u_h w}{\partial x_h} \right]_c - \left[\frac{\partial \tau_{3h}}{\partial x_h} \right]_c - \left\{ \frac{\partial w}{\partial t} \right\}_L - \left\{ \frac{\partial w w}{\partial z} \right\}_L - \left\{ \frac{\partial \tau_{33}}{\partial z} \right\}_L, \quad (\text{A4})$$

537 where M_c is the mass flux. The Leibniz terms are of significant magnitude. Besides, a
 538 more complicated behaviour of vertical velocity than assumed in the top-hat approach
 539 is present (e.g. Heus & Jonker, 2008), therefore lending itself less well for estimating the
 540 fractional entrainment rate (as compared to thermodynamic quantities).

541 To explain how different forcings under shear can contribute to differences in the
 542 updraft speeds, Fig. A1 shows these budget terms as deviations from the NS case. Pos-
 543 itive values indicate a stronger positive contribution to updraft speed (or a smaller neg-
 544 ative contribution). In particular, above 1 km, the FS and BS cases have a larger neg-
 545 ative P contribution (Fig. A1d), which is present at the same altitude where we see slower
 546 updraft speeds in the presence of shear (Fig. 8a). The differences in P are balanced mostly
 547 by differences in E (in the BS-4X case) or B (in the FS-4X case). The latter result from
 548 the different development of environmental temperature and humidity, as discussed in
 549 Section 4.1 and shown in Fig. 8c. The NS case with its strongest updrafts develops the
 550 deepest clouds and thus the warmest boundary layer, which reduces B , leading to a bal-
 551 ance in the budget over six hours. It thus appears that initial differences in updraft speeds
 552 develop due to differences in pressure gradients under shear, which are maintained through-
 553 out the simulation, as a balance with the buoyancy force is established.

554 Acknowledgments

555 We would like to thank Chris Bretherton and Bjorn Stevens for stimulating discussions
 556 as well as two anonymous reviewers for their comments that greatly improved the manuscript.
 557 This project has received funding from the European Research Council (ERC) under the
 558 European Union's Horizon 2020 research and innovation programme (Starting grant agree-
 559 ment no. 714918). ERA5 data were generated using Copernicus Climate Change Ser-

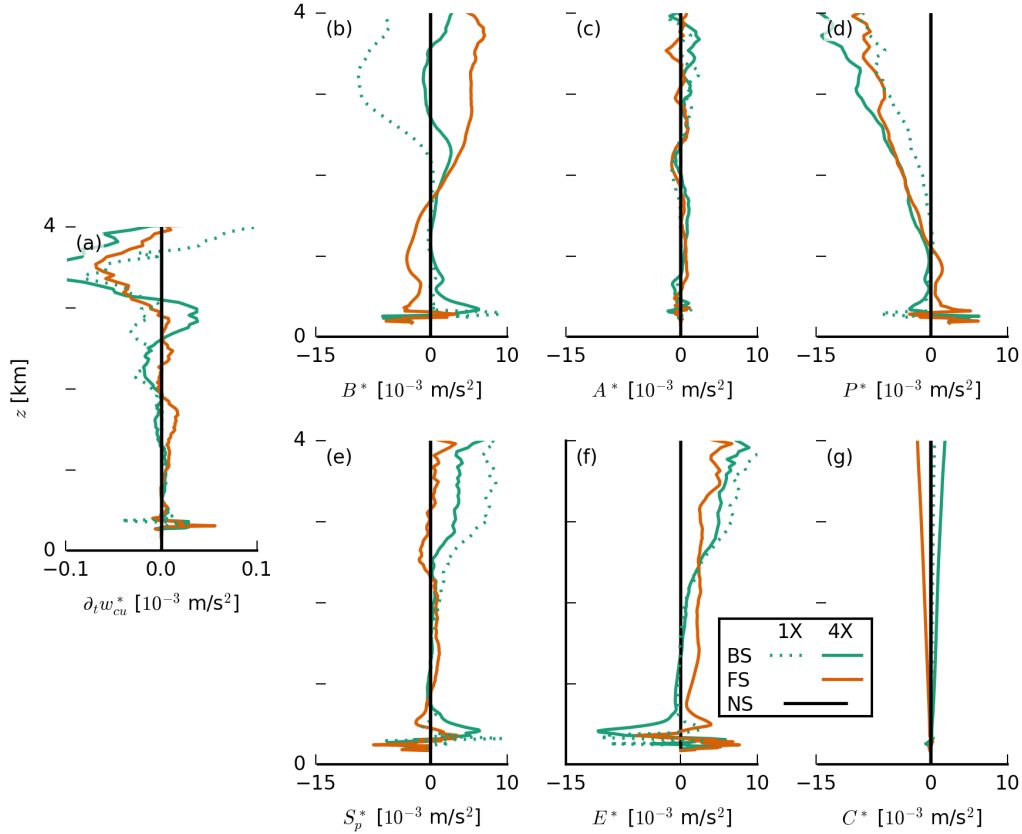


Figure A1. Slab-averaged profiles (averaged from 30 to 36 h of the simulations with prescribed surface fluxes) of the terms of the cloudy-updraft vertical-velocity budget (Eq. A1) plotted as differences from the NS case (indicated by the asterisks).

560 vice Information. Neither the European Commission nor ECMWF is responsible for any
 561 use that may be made of the Copernicus information or data in this publication. DALES
 562 is open-source software, which is distributed under the terms of the GNU GPL version
 563 3. The exact version of the code as well as the input files used in this work are available
 564 via <https://doi.org/10.5281/zenodo.4138940>.

565 **References**

566 Asai, T. (1964). Cumulus Convection in the Atmosphere with Vertical Wind Shear.
 567 *Journal of the Meteorological Society of Japan. Ser. II*, 42(4), 245–259.
 568 Bellon, G., & Stevens, B. (2012). Using the Sensitivity of Large-Eddy Simulations
 569 to Evaluate Atmospheric Boundary Layer Models. *Journal of the Atmospheric*

- 570 *Sciences*, 69(5), 1582–1601. doi: 10.1175/JAS-D-11-0160.1
- 571 Betts, A. K. (1975). Parametric Interpretation of Trade-Wind Cumulus Budget
572 Studies. *Journal of the Atmospheric Sciences*, 32(10), 1934–1945. doi: 10
573 .1175/1520-0469(1975)032(1934:PIOTWC)2.0.CO;2
- 574 Bony, S., & Dufresne, J.-L. (2005). Marine boundary layer clouds at the heart of
575 tropical cloud feedback uncertainties in climate models. *Geophysical Research
576 Letters*, 32(20). doi: 10.1029/2005GL023851
- 577 Bony, S., Stevens, B., Ament, F., Bigorre, S., Chazette, P., Crewell, S., . . . Wirth,
578 M. (2017). EUREC4A: A Field Campaign to Elucidate the Couplings Be-
579 tween Clouds, Convection and Circulation. *Surveys in Geophysics*. doi:
580 10.1007/s10712-017-9428-0
- 581 Bony, S., Stevens, B., Held, I. H., Mitchell, J. F., Dufresne, J.-L., Emanuel, K. A.,
582 . . . Senior, C. (2013). Carbon Dioxide and Climate: Perspectives on a Sci-
583 entific Assessment. In G. R. Asrar & J. W. Hurrell (Eds.), *Climate Science
584 for Serving Society* (pp. 391–413). Dordrecht: Springer Netherlands. doi:
585 10.1007/978-94-007-6692-1_14
- 586 Bretherton, C. S., & Blossey, P. N. (2017). Understanding Mesoscale Ag-
587 gregation of Shallow Cumulus Convection Using Large-Eddy Simulation.
588 *Journal of Advances in Modeling Earth Systems*, 9(8), 2798–2821. doi:
589 10.1002/2017MS000981
- 590 Brown, A. R. (1999). Large-eddy simulation and parametrization of the effects of
591 shear on shallow cumulus convection. *Boundary-Layer Meteorology*, 91(1), 65–
592 80.
- 593 Brueck, M., Nuijens, L., & Stevens, B. (2015). On the Seasonal and Synoptic
594 Time-Scale Variability of the North Atlantic Trade Wind Region and Its Low-
595 Level Clouds. *Journal of the Atmospheric Sciences*, 72(4), 1428–1446. doi:
596 10.1175/JAS-D-14-0054.1
- 597 Daleu, C. L., Woolnough, S. J., & Plant, R. S. (2012). Cloud-Resolving Model
598 Simulations with One- and Two-Way Couplings via the Weak Temperature
599 Gradient Approximation. *Journal of the Atmospheric Sciences*, 69(12), 3683–
600 3699. doi: 10.1175/JAS-D-12-058.1
- 601 de Roode, S. R., Siebesma, A. P., Jonker, H. J. J., & de Voogd, Y. (2012).
602 Parameterization of the Vertical Velocity Equation for Shallow Cumu-

- 603 lus Clouds. *Monthly Weather Review*, 140(8), 2424–2436. doi: 10.1175/
604 MWR-D-11-00277.1
- 605 Fedorovich, E., & Conzemius, R. (2008). Effects of wind shear on the atmospheric
606 convective boundary layer structure and evolution. *Acta Geophysica*, 56(1),
607 114–141. doi: 10.2478/s11600-007-0040-4
- 608 Grabowski, W. W. (1998). Toward Cloud Resolving Modeling of Large-Scale Trop-
609 ical Circulations: A Simple Cloud Microphysics Parameterization. *Journal of*
610 *the Atmospheric Sciences*, 55(21), 3283–3298. doi: 10.1175/1520-0469(1998)
611 055(3283:TCRMOL)2.0.CO;2
- 612 Heus, T., & Jonker, H. J. J. (2008). Subsiding Shells around Shallow Cumulus
613 Clouds. *Journal of the Atmospheric Sciences*, 65(3), 1003–1018. doi: 10.1175/
614 2007JAS2322.1
- 615 Heus, T., van Heerwaarden, C. C., Jonker, H. J. J., Siebesma, P. A., Axelsen, S.,
616 van den Dries, K., ... Vilà-Guerau de Arellano, J. (2010). Formulation
617 of the Dutch Atmospheric Large-Eddy Simulation (DALES) and overview
618 of its applications. *Geoscientific Model Development*, 3(2), 415–444. doi:
619 10.5194/gmd-3-415-2010
- 620 Hildebrand, P. H. (1998). Shear-Parallel Moist Convection over the Tropical Ocean:
621 A Case Study from 18 February 1993 TOGA COARE. *Monthly Weather Re-*
622 *view*, 126(7), 1952–1976. doi: 10.1175/1520-0493(1998)126(1952:SPMCOT)2.0
623 .CO;2
- 624 Hill, G. E. (1968). On the orientation of cloud bands. *Tellus*, 20(1), 132–137. doi:
625 10.3402/tellusa.v20i1.9936
- 626 Khanna, S., & Brasseur, J. G. (1998). Three-Dimensional Buoyancy- and Shear-
627 Induced Local Structure of the Atmospheric Boundary Layer. *Journal of the*
628 *Atmospheric Sciences*, 55(5), 710–743. doi: 10.1175/1520-0469(1998)055(0710:
629 TDBASI)2.0.CO;2
- 630 Klein, S. A., Hall, A., Norris, J. R., & Pincus, R. (2017). Low-Cloud Feedbacks
631 from Cloud-Controlling Factors: A Review. *Surveys in Geophysics*, 38(6),
632 1307–1329. doi: 10.1007/s10712-017-9433-3
- 633 Koren, I., Remer, L. A., Altaratz, O., Martins, J. V., & Davidi, A. (2010). Aerosol-
634 induced changes of convective cloud anvils produce strong climate warming.
635 *Atmos. Chem. Phys.*, 10(10), 5001–5010.

- 636 LeMone, M. A., & Pennell, W. T. (1976). The Relationship of Trade Wind Cu-
 637 mulus Distribution to Subcloud Layer Fluxes and Structure. *Monthly Weather*
 638 *Review*, *104*(5), 524–539. doi: 10.1175/1520-0493(1976)104<0524:TROTWC>2
 639 .0.CO;2
- 640 Li, Z., Zuidema, P., & Zhu, P. (2014). Simulated Convective Invigoration Processes
 641 at Trade Wind Cumulus Cold Pool Boundaries. *Journal of the Atmospheric*
 642 *Sciences*, *71*(8), 2823–2841. doi: 10.1175/JAS-D-13-0184.1
- 643 Malkus, J. S. (1949). Effects of wind shear on some aspects of convection.
 644 *Transactions, American Geophysical Union*, *30*(1), 19. doi: 10.1029/
 645 TR030i001p00019
- 646 Malkus, J. S. (1963). Cloud Patterns over Tropical Oceans. *Science*, *141*(3583), 767–
 647 778. doi: 10.1126/science.141.3583.767
- 648 Morrison, H., & Peters, J. M. (2018). Theoretical Expressions for the Ascent Rate of
 649 Moist Deep Convective Thermals. *Journal of the Atmospheric Sciences*, *75*(5),
 650 1699–1719. doi: 10.1175/JAS-D-17-0295.1
- 651 Neggers, R. A., Jonker, H. J., & Siebesma, A. P. (2003). Size statistics of cumulus
 652 cloud populations in large-eddy simulations. *Journal of the Atmospheric Sci-*
 653 *ences*, *60*(8), 1060–1074. doi: 10.1175/1520-0469(2003)60<1060:SSOCCP>2.0
 654 .CO;2
- 655 Nuijens, L., & Stevens, B. (2012). The Influence of Wind Speed on Shallow Ma-
 656 rine Cumulus Convection. *Journal of the Atmospheric Sciences*, *69*(1), 168–
 657 184. doi: 10.1175/JAS-D-11-02.1
- 658 Park, S.-B., Böing, S., & Gentine, P. (2018). Role of Surface Friction on Shallow
 659 Nonprecipitating Convection. *Journal of the Atmospheric Sciences*, *75*(1),
 660 163–178. doi: 10.1175/JAS-D-17-0106.1
- 661 Parker, D. J. (1996). Cold pools in shear. *Quarterly Journal of the Royal Meteorolo-*
 662 *gical Society*, *122*(535), 1655–1674. doi: 10.1256/smsqj.53508
- 663 Parker, M. D. (2010). Relationship between System Slope and Updraft Intensity
 664 in Squall Lines. *Monthly Weather Review*, *138*(9), 3572–3578. doi: 10.1175/
 665 2010MWR3441.1
- 666 Pastushkov, R. S. (1975). The effects of vertical wind shear on the evolution of
 667 convective clouds. *Quarterly Journal of the Royal Meteorological Society*,
 668 *101*(428), 281–291. doi: 10.1002/qj.49710142811

- 669 Peters, J. M. (2016). The Impact of Effective Buoyancy and Dynamic Pressure Forc-
 670 ing on Vertical Velocities within Two-Dimensional Updrafts. *Journal of the At-*
 671 *mospheric Sciences*, *73*(11), 4531–4551. doi: 10.1175/JAS-D-16-0016.1
- 672 Peters, J. M., Hannah, W., & Morrison, H. (2019). The Influence of Vertical Wind
 673 Shear on Moist Thermals. *Journal of the Atmospheric Sciences*, *76*(6), 1645–
 674 1659. doi: 10.1175/JAS-D-18-0296.1
- 675 Riehl, H., Yeh, T. C., Malkus, J. S., & La Seur, N. E. (1951). The north-east trade
 676 of the Pacific Ocean. *Quarterly Journal of the Royal Meteorological Society*,
 677 *77*(334), 598–626.
- 678 Robe, F. R., & Emanuel, K. A. (2001). The Effect of Vertical Wind Shear on Ra-
 679 diative–Convective Equilibrium States. *Journal of the Atmospheric Sciences*,
 680 *58*(11), 1427–1445. doi: 10.1175/1520-0469(2001)058(1427:TEOVWS)2.0.CO;
 681 2
- 682 Romps, D. M., & Charn, A. B. (2015). Sticky Thermals: Evidence for a Dominant
 683 Balance between Buoyancy and Drag in Cloud Updrafts. *Journal of the Atmo-*
 684 *spheric Sciences*, *72*(8), 2890–2901. doi: 10.1175/JAS-D-15-0042.1
- 685 Rotunno, R., Klemp, J. B., & Weisman, M. L. (1988). A Theory for Strong, Long-
 686 Lived Squall Lines. *Journal of the Atmospheric Sciences*, *45*(3), 463–485. doi:
 687 10.1175/1520-0469(1988)045(0463:ATFSSL)2.0.CO;2
- 688 Salesky, S. T., Chamecki, M., & Bou-Zeid, E. (2017). On the Nature of
 689 the Transition Between Roll and Cellular Organization in the Convec-
 690 tive Boundary Layer. *Boundary-Layer Meteorology*, *163*(1), 41–68. doi:
 691 10.1007/s10546-016-0220-3
- 692 Sathiyamoorthy, V., Pal, P. K., & Joshi, P. C. (2004). Influence of the Upper-
 693 Tropospheric Wind Shear upon Cloud Radiative Forcing in the Asian
 694 Monsoon Region. *Journal of Climate*, *17*(14), 2725–2735. doi: 10.1175/
 695 1520-0442(2004)017(2725:IOTUWS)2.0.CO;2
- 696 Siebesma, A. P., & Cuijpers, J. W. M. (1995). Evaluation of Parametric Assump-
 697 tions for Shallow Cumulus Convection. *Journal of the Atmospheric Sciences*,
 698 *52*(6), 650–666. doi: 10.1175/1520-0469(1995)052(0650:EOPAFS)2.0.CO;2
- 699 Sykes, R. I., & Henn, D. S. (1989). Large-Eddy Simulation of Turbulent Sheared
 700 Convection. *Journal of the Atmospheric Sciences*, *46*(8), 1106–1118. doi: 10
 701 .1175/1520-0469(1989)046(1106:LESOTS)2.0.CO;2

- 702 Thorpe, A. J., Miller, M. J., & Moncrieff, M. W. (1982). Two-dimensional con-
 703 vection in non-constant shear: A model of mid-latitude squall lines. *Quarterly*
 704 *Journal of the Royal Meteorological Society*, *108*(458), 739–762. doi: 10.1002/
 705 qj.49710845802
- 706 Tian, Y., Kuang, Z., Singh, M. S., & Nie, J. (2019). The Vertical Momentum
 707 Budget of Shallow Cumulus Convection: Insights From a Lagrangian Perspec-
 708 tive. *Journal of Advances in Modeling Earth Systems*, *11*(1), 113–126. doi:
 709 10.1029/2018MS001451
- 710 Vial, J., Bony, S., Stevens, B., & Vogel, R. (2017). Mechanisms and Model Diversity
 711 of Trade-Wind Shallow Cumulus Cloud Feedbacks: A Review. *Surveys in Geo-*
 712 *physics*, *38*(6), 1331–1353. doi: 10.1007/s10712-017-9418-2
- 713 Vogel, R., Nuijens, L., & Stevens, B. (2016). The role of precipitation and
 714 spatial organization in the response of trade-wind clouds to warming.
 715 *Journal of Advances in Modeling Earth Systems*, *8*(2), 843–862. doi:
 716 10.1002/2015MS000568
- 717 Weisman, M. L., & Rotunno, R. (2004). “A Theory for Strong Long-Lived Squall
 718 Lines” Revisited. *Journal of the Atmospheric Sciences*, *61*, 361–382.
- 719 Wyant, M. C., Bretherton, C. S., & Blossey, P. N. (2018). The Sensitivity of
 720 Numerical Simulations of Cloud-Topped Boundary Layers to Cross-Grid
 721 Flow. *Journal of Advances in Modeling Earth Systems*, *10*(2), 466–480. doi:
 722 10.1002/2017MS001241
- 723 Yamaguchi, T., Feingold, G., & Kazil, J. (2019). Aerosol-Cloud Interactions in
 724 Trade Wind Cumulus Clouds and the Role of Vertical Wind Shear. *Jour-*
 725 *nal of Geophysical Research: Atmospheres*, *124*(22), 12244–12261. doi:
 726 10.1029/2019JD031073
- 727 Young, G. S. (1988). Turbulence Structure of the Convective Boundary Layer.
 728 Part III: The Vertical Velocity Budgets of Thermals and Their Environ-
 729 ment. *Journal of the Atmospheric Sciences*, *45*(14), 2039–2050. doi:
 730 10.1175/1520-0469(1988)045<2039:TSOTCB>2.0.CO;2